Solar Energy 264 (2023) 111989

Contents lists available at ScienceDirect

Solar Energy

journal homepage: www.elsevier.com/locate/solener

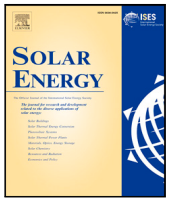

Optical measurements and flow modeling to characterize solid volume fractions in gravity-driven particle curtains

Theo A. Rulko [a,1], Bingjia Li [b,2], Brandon Surhigh [b,2], J. Michael Mayer [b], Rohini Bala Chandran [b,*]

[a] Aerospace Engineering, University of Michigan, Francois-Xavier Bagnoud Bldg. 1320 Beal Ave., Ann Arbor, MI, 48109, USA
[b] Mechanical Engineering, University of Michigan, G.G. Brown Laboratory, 2350 Hayward St., Ann Arbor, MI, 48109, USA

ARTICLE INFO

Dataset link: https://doi.org/10.17632/n69bss6bfg

Keywords:
Solid volume fraction
Particle curtain
Thermopile
Discrete element method
Monte Carlo ray tracing
Beer's law

ABSTRACT

Solid volume fraction is a defining characteristic of multiphase gas–solid flows. In the case of gravity-driven particle curtains, it changes significantly along the flow direction. This has implications for the performance of falling-particle solar receivers, which use particle curtains to capture and store heat from concentrated sunlight. This study reports on the characterization of solid volume fraction as a function of height in gravity-driven particle curtains using optical techniques and simulations performed with a discrete element method (DEM) model. The experimental domain is a hopper-fed vertical channel, and the modeling domain is designed to match the experimental setup. Solid volume fraction was obtained from experimentally measured transmittance using two techniques: (1) a thermopile detector paired with a visible light source and (2) a high-speed camera. The DEM simulations were calibrated by identifying the coefficient of static friction between particles that resulted in equivalent mass flow rates to the experiments. All techniques, including an analytical model derived from first principles and empirical relationships, showed very similar trends of solid volume fraction decreasing along the flow direction, where it drops off rapidly initially before leveling off in a power law relationship. Both experimental and computational tests were performed with 1 mm and 2 mm particles, and solid volume fraction is found to decrease with increasing particle size at any location in the channel. Furthermore, the solid volume fractions calculated from transmittance measurements were found to be sensitive to the optical properties of the particles through Monte Carlo ray tracing simulations. To account for this effect, a new scale factor dependent on particle reflectivity is derived, which leads to significantly improved agreement between experimental and simulated results. A simple, closed-form equation is proposed to transform measured transmittance to a solid volume fraction while accounting for particle reflectivities. Even though solid volume fractions above 0.1 were not measured in this study, the technique developed is suitable to measure even larger solid volume fractions, especially for more reflective particles.

1. Introduction

The next generation of concentrated solar power (CSP) plants promises improved efficiency and lower cost, partly through the use of solid ceramic particles as a medium to capture, transfer, and store heat in place of molten salts. Gas–solid multiphase flows, including fluidized beds, moving packed beds, and gravity-driven particle curtains, marry the advantages of high thermal capacity and thermal conductivities in solids with enhanced mass, momentum, and heat transfer rates by achieving fluid-like behavior, making them ideal for heat transfer and thermal energy storage applications [1–3]. This study focuses on experimental measurements to characterize solid volume fractions (equivalently solids concentration) in a gravity-driven flow of particles.

Many techniques that vary widely in cost and complexity have been developed to measure solid volume fraction in gas–solid multiphase flows. The applicability of a technique depends on many factors, including the range of solid volume fractions to be measured, the average particle size and size distribution, and the physical properties (gravimetric, optical, electrical, magnetic, etc.) of the solid and fluid phases. Nieuwland et al. present a comprehensive summary of the most common measurement techniques [4]. The most direct approach to quantifying solid volume fraction is a gravimetric technique that utilizes quick closing valves to capture the solid phase, which can be used to deduce solids concentration and a solid volume fraction [5]. This technique can theoretically be used for any range of solid volume

* Corresponding author.
E-mail address: rbchan@umich.edu (R. Bala Chandran).
[1] Present address: Department of Aeronautics & Astronautics, Massachusetts Institute of Technology, 500 Technology Square, Cambridge, MA, 02139, USA.
[2] Equal contributors.

https://doi.org/10.1016/j.solener.2023.111989
Received 4 April 2023; Received in revised form 8 August 2023; Accepted 30 August 2023
Available online 28 September 2023

fractions, but it is severely limiting as it requires a complete stoppage of flow to make the measurement. Additionally, it is not able to determine the spatial or temporal evolution of solid volume fractions. In fluidized bed applications that do not require a high spatial resolution, manometric measurements are well-suited to determine average solid volume fractions in the range 0.2–0.4 [3,5–7]. In this technique, the pressure drop is measured for the fluidized mixture over a selected length of a tube section and related to the volume fractions of the particles and the fluid phase.

Optical techniques encompass various methodologies but can be grouped into two major categories. The first group involves the measurement of a transmitted or reflected intensity from a light source by the multiphase medium and correlates this measurement to a solid volume fraction. A common way to do this is to instrument flow channels with fiber optic probes that transmit light from an emitting source, such as a laser diode, and to transmit light back to a detector, such as a photodiode, at a location in the channel where solid volume fraction is being measured [4,8–12]. In one arrangement, optical fiber probes measure the transmittance of the light through the multiphase medium, which can be related to solid volume fraction based on the extinction behavior of the medium [13]. Prior studies have used different sources of light including lasers, ultraviolet (UV) lamps, and light panels, with light detection being accomplished by photodiodes and thermopiles [14–16]. The maximum volume fraction measurable with the transmittance approach is strongly dependent on the particle size, particle optical properties, and the optical path length, but generally this method has been limited to dilute flows with solid volume fractions up to 0.25 [4]. In contrast, optical techniques that operate on the principle of reflectance can measure denser packing fractions up to 0.6, by establishing specialized calibration curves [12].

The second group of optical techniques is those that capture images of the flow and determine a solid volume fraction through post-processing [17–20]. High-speed cameras capture a 2D projection of the flow, and image processing strategies are used to extract an opacity, which can be related to the solid volume fraction. However, like transmittance measurements, this technique is better suited for dilute flows. With stereoscopic imaging to generate 3D reconstructions of the flow, particle positions, velocities, and ultimately a volume fraction can be obtained. However, this is a challenging procedure that is also limited by the necessity of optical access from multiple dimensions. For instance, Spinewine et al. were restricted to near-wall particle flows in applying stereoscopic imaging [20]. Moreover, high-speed cameras can pose a cost barrier depending on the required frame rate and resolution. Recently, much work has been done to characterize granular flows with other forms of electromagnetic radiation including magnetic resonance imaging (MRI), positron emission tomography (PET), and ultrafast X-ray computed tomography [21–26]. These techniques are extremely powerful in that they provide quantitative three-dimensional data that can be used to probe nearly any regime of granular flow and range of solid volume fractions at rapid frequencies, e.g., 8 kHz [22]. However, these methods often involve high capital costs and extensive facilities development to perform in-situ imaging. In addition, applying these techniques requires materials to have select properties, e.g., particles used in MRI techniques must provide a strong signal in response to the magnetic fields.

Non-intrusive electrical capacitance and impedance measurements have been successfully used in two- and three-phase fluidized beds and for dense flows with solid volume fractions up to 0.6 [27–33]. In this technique, the dielectric permittivity of the multiphase medium is dictated by the concentration of solids present, which affects the measured capacitance. However, the accuracy of these predictions is strongly reliant on models that relate the change in permittivity to a solid volume fraction of the mixture, with challenges stemming from permittivity also being dependent on the spatial distributions of particles [34]. While this approach has been expanded to perform three-dimensional reconstructions using electrical capacitance volume tomography (ECVT), it often requires co-optimization of sensor shape, electrode configurations, and the number of electrodes, along with expensive computations to obtain high-fidelity quantitative data [34,35].

Overall, optical and electrical capacitance-based flow characterization techniques are robust and have been extensively used to perform 2D and 3D quantification of solid volume fractions for multiphase flows. However, many of these techniques are limited in adoption by the broader research community due to expensive facilities development, including safety protocols (e.g., X-ray techniques), and/or complex post-processing steps for data calibration and image processing. Furthermore, performing flow characterization using advanced optical techniques (X-ray, MRI, PET, etc.) can require a dedicated test setup with different dimensions and possibly different materials than those of interest to achieve property compatibility. For example, it may be desirable to perform high-speed video imaging measurements in conjunction with gravimetric or electrical capacitance measurements [32].

Motivated by these factors, this study explores a relatively simple, low-cost, optical transmittance measurement technique to characterize solid volume fractions for the gravity-driven flow of millimeter-sized ceramic particles. A visible light source is coupled to a thermopile detector to measure transmitted intensity by the particle curtain at various locations along the flow direction. To deduce a solid volume fraction from the measured transmittance, prior work has extensively applied the Beer–Bouguer–Lambert law (henceforth referred to as Beer's law), which is only applicable for homogeneous and purely absorbing media with normal illumination [36]. A unique contribution from this study is that these assumptions were tested with ray tracing simulations, informing the governing relationships between measured transmittance, optical properties of the particles, and the solid volume fraction. To provide further credibility to this approach and insights on experimental data, estimated solid volume fractions are compared with (a) predictions from a discrete element model of particle flow and (b) high-speed video camera shadowgraphy.

2. Experimental and modeling approaches

2.1. Experimental methods

Particle curtain tests were conducted using a laboratory-scale flow chamber (Fig. 1). This was fabricated from a combination of off-the-shelf and custom-fabricated sheet metal parts. It consists of a frustum-shaped hopper with 45° walls that feeds particles through a 7.5 mm × 150 mm discharge slot into a 9.58 mm × 150 mm × 500 mm channel, which constrains the width of the curtain. Manual slide gates at the top and bottom of the channel allow flow to be controlled, while transparent acrylic windows along its sides allow optical access. A load cell mounted under the collection bucket at the channel base provides mass flow data as a function of time and is used to find the mass flow rate.

Commercially available, highly spherical porcelain particles from Raytech Industries [37] were used for all experiments. These have bulk density of $\rho_p = 2650\ \mathrm{kg/m^3}$ and were obtained in nominal sizes of 1 mm and 2 mm diameters. Their average size and size distribution differ somewhat from those specified by the manufacturer; the 1 mm particles have an average diameter $d_p = 1.23$ mm and are normally distributed with standard deviation $\sigma_d = 0.1$ mm, while the 2 mm particles have an average diameter $d_p = 2.18$ mm and are normally distributed with $\sigma_d = 0.1$ mm. The average diameter was determined by taking an arithmetic mean of a sample of particle diameters. The size distribution of particles was quantified using image processing techniques, as described in Appendix A. Tests were conducted with small batches of particles at a time, at steady mass flow rates. The flow rates were measured with an iW-8x8-10M-DI-1000U load cell from Loadstar Sensors [38]. The duration of each test was 25 to 35 seconds.

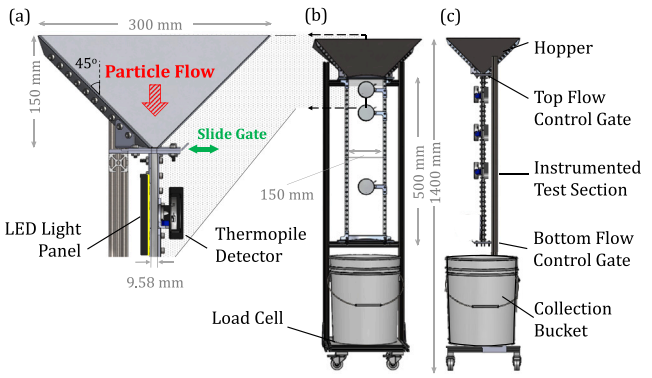

Fig. 1. Lab-scale flow chamber for gravity-driven particle flow experiments. (a) Cross-sectional detail view of the hopper and the top slide gate. (b) Front view of flow chamber. (c) Side view of flow chamber.

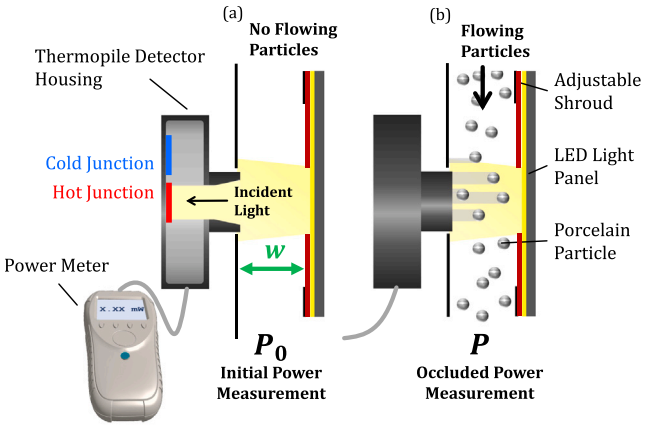

Fig. 2. Illustration of the thermopile-based measurement technique. (a) Cross-sectional view of the detector and light source measuring initial power P_0 transmitted through the empty flow channel, with hot and cold junctions shown. (b) Exterior view of the detector measuring occluded transmitted power P through the particle curtain. Transparent acrylic walls encase the flowing particles. (For interpretation of the references to color in this figure legend, the reader is referred to the web version of this article.)

Even though millimeter-size particles were used in this study, the transmittance-based measurement technique is agnostic to particle size. While sub-millimeter particles are typically considered for solar receiver applications, porcelain particles with high sphericity are readily commercially available in well-controlled size distributions (starting at 1 mm) with consistent surface and optical properties. This allows for a more controlled comparison of the influence of particle size on solid volume fraction. Additionally, geometric tolerances in the experimental setup are not conducive to the use of sub-millimeter particle sizes, which lead to jamming at the slide gate and more material loss during testing.

All tests were performed for cold flows of particles at room temperature. However, these results are expected to be generally applicable even with hot particles flowing through the channel. This is because there is little interaction between the particles once they exit the hopper, and therefore the solid volume fraction profile is not expected to be greatly influenced by particle temperatures in this curtain flow regime. With hot particles, measuring transmittance using a thermopile is challenging due to its sensitivity to infrared energy.

2.1.1. Thermopile measurements

To directly measure the intensity of light transmitted through the curtain, an LED light source (Neewer NL 480), thermopile detector (Newport 919P-003-10), and power meter (Newport 843-R-USB) were used [39,40]. Thermopiles are composed of several thermocouples connected in series, each with one junction exposed to an absorbing surface and the other exposed to a heat sink. The hot junction is coated with a high-absorptivity coating (red junction in Fig. 2), and the cold junction is shielded from incident light (blue junction in Fig. 2). The differential voltage output from the thermopile is used to determine the incident radiative heat flux onto the absorbing surface of the hot junction by the power meter connected to the sensor; the cold junction corrects for background error due to temperature changes in the sensor housing [40,41].

The thermopile selected for this experiment has a nearly-flat spectral response over a large range of wavelengths (0.2–11 μm), including the spectrum of the light source used in this study (0.5–0.9 μm). It has a sensor area of 70.9 mm^2. Its calibration was verified experimentally by constraining the field of view of the sensor and illuminating it with a light source of known intensity, and then validating the relationship between the total measured power and the illuminated area. Transmittance through the curtain was found by the ratio of the power measured when particles are flowing in the channel (Fig. 2b) to when it is empty (Fig. 2a). Since the detector area is constant, this power ratio is equal to the transmittance through the particle curtain. The thermopile measurements were found to be sensitive to the size of the light source used to illuminate the detector: larger, more diffuse light sources yielded higher transmittance while smaller, more collimated light sources yielded lower transmittance under the same flow conditions. This is because a light source with a smaller area that approaches the viewing angle of the thermopile helps minimize stray reflections from outside the field of view. Therefore, to constrain the illumination area and further collimate the beam from the light source, an adjustable shroud made of black, insulating rubber foam was mounted between the light source and flow chamber, as shown in Fig. 2.

Tests were performed for the same particle size with the thermopile positioned at distinct locations along the flow direction. The top-most locations where transmittance was recorded were 23.4 mm and 55 mm below the top slide gate (Fig. 1) for the thermopile and high-speed camera, respectively (see Section 2.1.2). While widening of the particle curtain thickness is expected, the particle-tracking model predictions show that this effect is limited to within 15 mm below the top slide gate. Therefore, the particle curtain width has already expanded to the width of the channel of 9.5 mm for all measured transmittance data.

2.1.2. Front-lit high-speed camera measurements

To compare against a method widely used in literature, a camera-based approach for measuring solid volume fraction, similar to that used by Kim et al. [30] and Ho et al. [42], was also implemented. A Vision Research Phantom v711 high-speed digital video camera, equipped with a Nikon zoom lens, was used to image the particle curtain at a resolution of 1280 × 800 at 5 kHz. With these high framerates, the particle curtain was imaged without the challenges of motion blur. The camera was placed on a tripod approximately 1.5 m from the chamber, such that the first 300 mm of the chamber were within the field of view, as shown in Fig. 3a. Unlike the method adopted by Kim et al. where the particle curtain was back-lit by a diffuse reflector, the chamber was front-lit by a pair of bright LED strobe lights, at a frequency synchronized to that of the camera. A dark fabric was placed behind the chamber to maximize the contrast between the white particles and the background.

Compared to the back-lit approach, the front-lit approach is more sensitive to the absorptance and reflectivity of the particles, and can suffer from glare on the flow chamber windows. To combat these effects, the videos were processed in MATLAB via a binarization scheme using the Image Processing Toolkit. This scheme classifies each pixel as a particle or background according to a threshold value, then sets

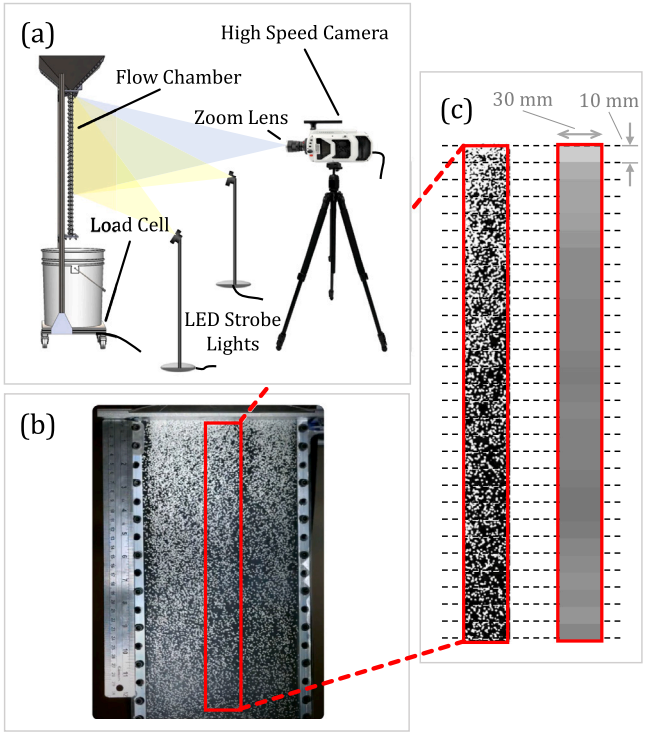

Fig. 3. Implementation details for the camera-based approach, shown for 1 mm particles. (a) Experimental apparatus, including the flow chamber, load cell, pair of LED strobe lights, zoom lens, and high-speed camera. (b) Sample video frame, with the region of interest boxed. (c) Sample processing steps, including binarization (left) and averaging (right) over bins of 10 mm height.

each to pure white or black, respectively. The threshold was computed independently in each bin via Otsu's method, to combat localized glare from the strobe lights on the chamber window which results in non-uniform background brightness [43]. This process renders the front- and back-lit shadowgraphy methods roughly equivalent, though the binarization process in the front-lit approach may introduce an additional source of error that is not present in the back-lit approach. Both approaches did not consider particle reflectance and treat the particles as totally absorbing.

To obtain transmittance data, each recorded frame was converted to a grayscale image and processed to isolate a region of interest in the center of the channel with a width of 30 mm, corresponding to the location where transmittance is measured by the thermopile detector (Fig. 3b). The region was then vertically divided into 28 bins (h_{bin} = 10 mm) along the height of the channel with $h_{bin} \gg d_p$ (Fig. 3c). Within individual bins, the data were spatially averaged to compute a mean pixel brightness and therefore transmittance and solid volume fraction as a function of height. A time average of transmittance in each bin was obtained by averaging over all frames recorded for a flow test (see Appendix B). Six tests for each particle size were performed and imaged with the high-speed camera, such that a 95% confidence interval on transmittance could be found using the Student's t-distribution.

2.1.3. Solid volume fraction estimation from measurements

The transmittance of light, T, through a particle curtain is related to the extinction coefficient, β, through Beer's law:

$$T = \exp(-\tau) \quad \text{where} \quad \tau = \beta W \tag{1}$$

and where W is the optical path-length (in this case is the curtain/channel thickness), and τ is the corresponding non-dimensional optical thickness dependent on particle size, solid volume fraction, and the path length. For Eq. (1) to be applicable, a homogeneous medium that is perfectly absorbing with normal incidence of light needs to be assumed [36]. However, the porcelain particles reflect a significant portion of the incident light from the LED panel, and the flow is not homogeneous. Therefore, using Eq. (1) directly is not appropriate for this study. To determine the extinction coefficient for the case of large, opaque particles (where $d_p \gg \lambda$), independent scattering is commonly assumed, where scattering on the surface of one particle remains unaffected by the presence of neighboring particles. The independent scattering theory extinction coefficient, β_{ind} can be expressed as a linear function of the solid volume fraction ϕ:

$$\beta_{\text{ind}} = \frac{3\phi}{2d_p} \tag{2}$$

However, for solid volume fractions larger than 6%, corrections must be made to the extinction coefficient due to dependent scattering; i.e., reflections from neighboring particles also influencing radiative transport in the particulate medium [44–47]. Hence, the independent scattering theory extinction coefficient, β_{ind}, is corrected with a scale factor, S_ϕ, as determined by Singh & Kaviany for spherical, opaque particles with $\phi < 0.7$ [46]:

$$\beta = S_\phi\ \beta_{\text{ind}},\ S_\phi\ = 1 + 1.84\phi - 3.15\phi^2 + 7.20\phi^3 \tag{3}$$

While additional influence of the spatial distribution of particles on dependent scattering has been shown by Li & Bala Chandran [47], Frankel et al. [13], and Chen et al. [48], a random distribution of particles is a reasonable assumption for the flow considered in this study.

Using results from direct ray tracing simulations integrated with a particle flow model (Section 2.2.3), this study will obtain a modified Beer's law expression, (as will be shown in Eq. (11)) that explicitly also depends on particle reflectivity.

2.2. Modeling methods

The solid volume fraction, ϕ, is expected to decrease as a function of vertical height through the channel, z. This dependence is quantified with two modeling approaches. In a relatively simplistic calculation, a force balance was performed for a single particle combined with empirical correlations for particle discharge rates from the hopper. In another model, multi-particle position tracking was performed using discrete element modeling.

2.2.1. Single particle force balance

By balancing the gravitational and drag forces in 1D, a reasonable approximation for the spatial variation of ϕ with z is obtained. The ordinary differential equation (ODE) in Eq. (4) governs the net acceleration of the particle, with the initial condition given in Eq. (5):

$$\frac{dv_p}{dt} = g - \frac{0.5\rho_{\text{air}} C_D A_p v_p^2}{m_p} \tag{4}$$

$$v_p(t=0) = v_{p0} \tag{5}$$

where v_{p0} is the initial particle velocity as it exits the hopper, ρ_{air} is the air density, A_p is the cross-sectional area of one particle, m_p is its mass, and C_D is the drag coefficient for a sphere. The latter is obtained from the empirical correlation reported by [49]:

$$C_D = \frac{24}{Re} + \frac{2.6\left(\frac{Re}{5.0}\right)}{1+\left(\frac{Re}{5.0}\right)^{1.52}} + \frac{0.411\left(\frac{Re}{2.63\times10^5}\right)^{-7.94}}{1+\left(\frac{Re}{2.63\times10^5}\right)^{-8.00}} + \frac{0.25\left(\frac{Re}{10^6}\right)}{1+\left(\frac{Re}{10^6}\right)} \tag{6}$$

where the Reynolds number is defined based on the particle size, $\text{Re} = \rho_{\text{air}} v_p d_p / \mu$, and ranges from $\mathcal{O}(10^1)$ to $\mathcal{O}(10^2)$. Note that μ is the dynamic viscosity of air. By conservation of mass and for a steady flow rate, $\dot{m}$, through the channel, the solid volume fraction is inversely proportional to particle velocity, v_p:

$$\phi = \frac{\dot{m}}{\rho_p A v_p} \tag{7}$$

Table 1
Table of relevant physical dimensions for measurement and modeling.

Symbol	Description
d_p = 1.23 or 2.18 mm	Particle diameter
W = 9.58 mm	Flow chamber width
L = 150 mm	Flow chamber length
H = 500 mm	Flow chamber height
$\overline{W}_s$ = 5.93 mm	Discharge slot width (average)
$W_{s,c}$ = 5.73 mm	Discharge slot width (at center)

Table 2
Table of derived dimensions.

Symbol	Description
$W_s^* = \overline{W}_s - k^* d_p$	Modified discharge slot width
$L^* = L - k^* d_p$	Modified discharge slot length
$A_p = \pi d_p^2/4$	Cross-sectional particle area
$A = LW$	Curtain cross-sectional area
$A_s = L\overline{W}_s$	Discharge slot area at hopper exit
$A_s^* = L^* W_s^*$	Modified discharge slot area
$P_s^* = 2L^* + 2W_s^*$	Modified discharge slot perimeter
$D_{sH}^* = 4A_s^*/P_s^*$	Modified hydraulic diameter

where ρ_p is the bulk particle density and A is the curtain cross-sectional area, defined by the depth and width of the flow channel.

The initial velocity as the particle exits the hopper is obtained by adapting the empirical Rose–Tanaka–Beverloo–Nedderman (R–T–B–N) correlation for hoppers with rectangular openings [50]:

$$v_{p0} = 0.74\sqrt{g D_{sH}^*} \tag{8}$$

where D_{sH}^* is the hydraulic diameter. The discharge slot area and perimeter, A_s^* and P_s^*, respectively, used to calculate hydraulic diameter (Tables 1, 2) are corrected for an empty zone near the slot edge, which has been observed empirically [51]. This correction is applied by subtracting $k^* d_p$ from each slot dimension, where $k^* = 1.15$ is a constant. For clarity, the physical dimensions are described in Table 1, while areas and other derived dimensions are described in Table 2. The R–T–B–N correlation is most accurate for particle diameters greater than 0.4 mm, below which drag effects become important, and where at least 6 particles fit across the width of the hopper opening [51].

Finally, the steady-state mass flow rate referenced in Eq. (7) is governed by the rate of discharge of particles from the hopper, which is obtained from the initial velocity estimated using the R–T–B–N correlation in Eq. (8) and the definition of mass flow rate:

$$\dot{m} = \rho_p \phi_0 A_s^* v_{p0} \tag{9}$$

where ϕ_0 is the initial solid volume fraction of particles in the hopper. Assuming an initial random packing of monodisperse spheres in the hopper, ϕ_0 is set equal to 0.625 [52]. The set of algebraic equations given in Eqs. (6)–(9) is solved along with the ODE in Eq. (4) to determine ϕ as a function of position, z.

2.2.2. Discrete element modeling for particle tracking

To perform multi-particle position tracking, LIGGGHTS [53], an open-source software to perform discrete element modeling (DEM), is used. The modeling domain (Fig. 4) is a hopper-channel geometry based on the experimental flow chamber (Fig. 1). The dimensions of the discharge slot are selected based on the geometry as manufactured; deformations in the manufactured hopper are non-uniform and greater in the center where the transmittance is measured. This leads to a modeled slot width, $W_{s,c}$ of 5.73 mm (Fig. 4 inset, Table 1). This choice results in the overall slot area being smaller than the manufactured slot area, while the width at the center matches the manufactured flow chamber.

In this DEM simulation, particle–particle and particle–wall collisions are computed based on the Hertzian theory - a spring-dashpot model. Normal and tangential components of contact forces are computed for

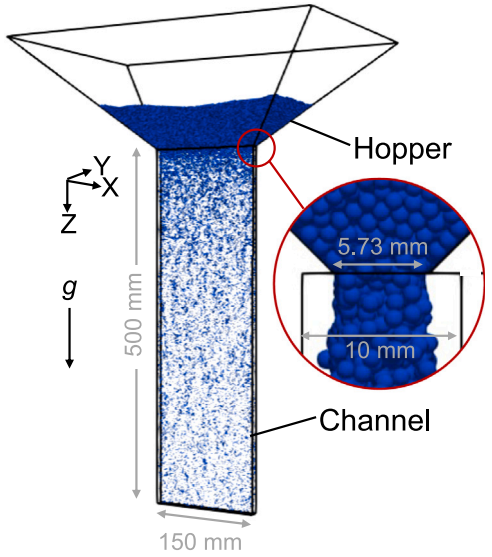

Fig. 4. Flow model used in DEM simulations, including a detailed view of the discharge slot that accounts for the deformation in the manufactured hopper.

Table 3
Particle geometric and material properties used in DEM simulations.

Parameter	Value
Particle density ρ (kg/m^3)	2760.5
Particle diameter d_p (mm)	1.23, 2.18
Young's modulus E (MPa)	5.00
Poisson's ratio υ	0.17
Coeff. of restitution, particle–particle ϵ_p	0.45
Coeff. of restitution, particle–wall ϵ_w	0.45
Coeff. of static friction, particle–particle $\mu_{s,pp}$	0.36
Coeff. of static friction, particle–wall $\mu_{s,pw}$	0.1

all particles. When the calculated tangential force exceeds the product of the friction coefficient and the normal force, i.e., $F_t > \mu_s F_n$, sliding is assumed to occur. The DEM time step is set to 2×10^{-5} s, which is smaller than the critical DEM time step (usually found to be 10% to 30% of the Rayleigh time step of 1.25×10^{-4} s that characterizes force propagation through one particle [53]). The effect of drag on particle flow was found to be negligible due to the short residence time of particles in the channel and the low viscosity of air. This was further confirmed by comparisons of analytical models with and without drag. The parameters implemented in this DEM model are reported in Table 3. Neither the particle–particle nor particle–wall rolling friction forces are modeled since their influences are expected to be negligible for the flow configuration investigated in this study [54].

The particles modeled in the DEM simulations are assumed to be spherical and monodisperse with an average diameter and particle density obtained from measurements (Appendix A). DEM simulations show that the influence of a polydisperse distribution on flow is negligible; comparable results are obtained with a monodisperse distribution with an average particle size obtained from the experimentally measured size distribution (Appendix C). While particle shape can significantly influence flow behavior [55], image analyses of particle samples show high sphericity and validate the choice of modeling particles as spheres. Additionally, particle surface roughness can influence friction and restitution coefficients, and therefore sensitivity of predictions to the friction coefficient is evaluated.

It is expected that DEM simulation results will be influenced by input values chosen for various model parameters, including the friction and restitution coefficients (Table 3) [54]. Therefore, baseline values are selected rationally and sensitivity analyses is performed for

specifically the particle–particle and particle–wall friction coefficients. An unrealistically small Young's modulus of $E = 5$ MPa was used for the particle force calculations, where the permitted range is 5 MPa to 1 GPa in LIGGGHTS [53]. This artificial reduction in Young's modulus has been applied in prior work and has been shown to have negligible influence on the flow behavior [56]. Additionally, this practice significantly lowers computational cost in particle tracking simulations, as the critical DEM time step, $\Delta t_{\mathrm{cr,\ DEM}}$ is inversely related to the Young's modulus ($\Delta t_{\mathrm{cr,\ DEM}} \propto 1/\sqrt{E}$) [57]. While particle–wall static friction has negligible influence on the flow behavior, the particle–particle friction coefficient has a significant effect on both the mass flow rate and the solid volume fraction distribution. Particle–particle friction coefficients in the range of 0 to 0.9 are modeled, which includes the values 0.5 to 0.72 reported in the literature for commercially available Carbobead HSP and CP ceramic particles for CSP applications [48,57]. A nominal restitution coefficient of 0.45 is assumed with the expectation that its influence on dilute particle curtain flows will be minimal. This is further supported by predictions that show less than 8% deviation in mass flow rates for a wide range of restitution coefficients ($\epsilon_p \in (0.05–0.85)$) in a more contact-driven flow of particles inside a hopper [54]. Rolling friction is neglected as its effects on dilute, particle curtain flows are expected to be insignificant.

To initialize the DEM calculations, 1.5 kg of particles are inserted in the hopper and given ~5 seconds to settle. Then, the particles are released into the channel until the hopper is empty. To obtain the solid volume fraction, ϕ, a few snapshots of the positions of particles in the channel are extracted from the simulations. The channel region is divided into 20 bins and the number of particles inside each bin, $N_{p,b}$, is counted. This bin height is selected to be much larger than the particle size ($H_b = 25$ mm $\approx 12–25 d_p$). The spatially-averaged solid volume fraction is computed with Eq. (10):

$$\phi_b = \frac{N_{p,b}\frac{\pi}{6}d_p^3}{LWH_b} \tag{10}$$

The approach of obtaining solid volume fraction from DEM simulations differs from the experimental techniques, which transform a measured transmittance to a solid volume fraction.

2.2.3. Transmittance dependence on particle reflectivities

Snapshots of particle positions from the DEM simulations are directly input to collision-based Monte Carlo ray tracing models to calculate transmittance for various particle reflectivities, R_p ranging from 0 (purely absorbing/black) to 0.99 (highly reflective). These results inform how measured transmittance can be converted to a solid volume fraction and its dependence on particle reflectivity. The flow channel is vertically divided into ten subdomains with a size of 10 mm × 150 mm × 50 mm subdomains (Fig. 5(a)). In each subdomain, 10^6 rays are launched parallel to the y-axis (normal to the x–z plane), as shown in Fig. 5(b). Rays are considered transmitted when they reach the opposite side of the channel from where they were launched. Surfaces normal to the z-axis are periodic boundaries, and the surfaces normal to the x-axis are purely absorbing walls.

Transmittance simulations require inputs for the reflectivity of the particles. The model treats particle reflectivity as a variable parameter, but reasonable estimates using experimental measurements are also obtained. Even though the total reflectivity of the porcelain particles is dependent on the spectrum of the light source, estimates for this value are made by measuring the spectral reflectivity of packed beds of the porcelain particles in a UV–Vis spectrophotometer (Shimadzu UV-2600). The particle beds exhibit reflectivity values between 0.5 and 0.6 throughout the visible spectrum, which includes most of the energy emitted by the light source (Fig. D.1). However, the reflectance measured for the bed of particles is expected to underestimate the reflectivity of individual particle surfaces because of multiple light scattering events within the bed.

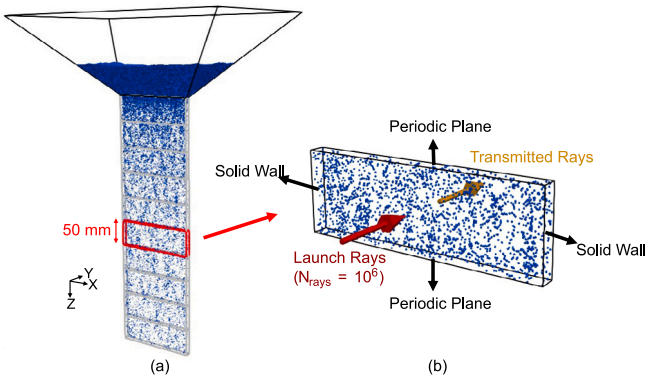

Fig. 5. (a) Division of the flow chamber into subdomains for ray tracing simulations with (b) an exploded view of the subdomain and the corresponding boundary conditions for ray tracing simulations.

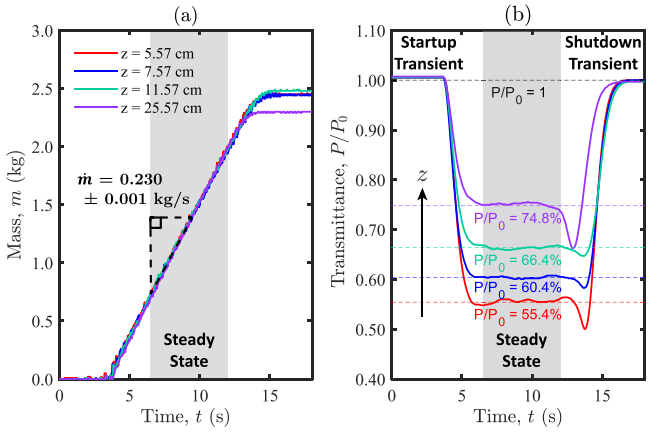

Fig. 6. (a) Load cell data and (b) normalized thermopile data for several representative flow tests of 1 mm particles at various distances z from the hopper. In (b), there is a slight decrease in initial power after the test. (For interpretation of the references to color in this figure legend, the reader is referred to the web version of this article.)

3. Results and discussion

3.1. Thermopile and load cell measurements

Representative experimental results for the synchronized thermopile and load cell measurements as a function of time and over various heights are presented for the 1 mm particles in Fig. 6. The load cell data (Fig. 6a) show that the mass flow rate into the channel is constant throughout the duration of a test, except during the shutdown period as the hopper empties. Mass flow rates of 0.230 ± 0.003 kg/s and 0.160±0.003 kg/s are measured for 1 and 2 mm particles, respectively. A high degree of repeatability was obtained for mass flow measurements over 40+ trials per particle size; the trial-to-trial variation based on the 95% confidence interval in flow rate is only 0.001 kg/s and 0.002 kg/s for 1 mm and 2 mm particles, respectively. This is less than the overall measurement uncertainty of 0.003 kg/s for both particle sizes. Since the number of particles loaded into the hopper was not strictly controlled between trials, some trials lasted for a shorter duration than others. For example, the trial at $z = 25.57$ mm for 1 mm particles (Fig. 6, purple line) has a shutdown transient that begins sooner and reaches a lower total mass of particles than other trials.

Four trials at each height for each particle size were performed to obtain the transmittance data as a function of height; a 95% confidence interval was computed via Student's t-distribution. The thermopile data (Fig. 6b) demonstrate that transmittance measured at a fixed

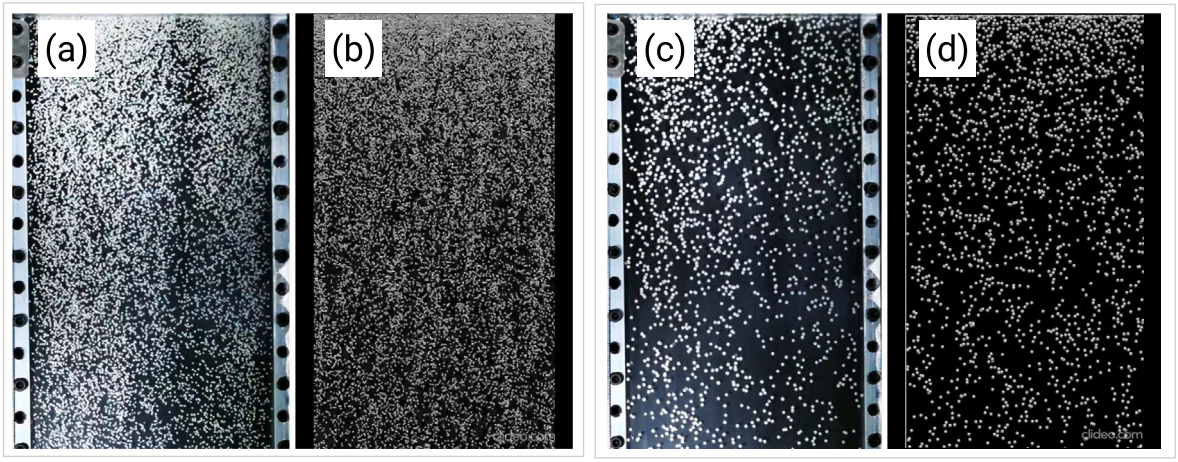

Fig. 7. Qualitative comparison of experimental (a, c) and simulated (b, d) curtain flow at a selected time instant. (a) and (b) show 1 mm particles, while (c) and (d) show 2 mm particles. Photos are generated by selecting a high-speed camera frame at steady state.

location varies with time, exhibiting a steep drop while particles are flowing. Transmittance oscillates very slightly about the mean even during the steady-state period (indicated by the gray shaded areas in Fig. 6). These oscillations are attributed to statistical variations in the flow due to the presence of many-particle interactions. A steep dip in transmittance is observed during shutdown transients. This is attributed to the clustering of particles in the center of the channel, where the thermopile is positioned, when the hopper is nearly empty, due to the inward slant of the hopper. Additionally, there is a very slight reduction in transmittance of the empty channel before and after a test, which is attributed to the accumulation of particle dust on the chamber windows.

Transmittance is obtained from the power measurements by normalizing the power measured when the particles are flowing, P (gray shaded areas) by the initial power, P_0, measured without any particles in the channel. P was found from steady-state data only, while P_0 was taken as the mean between initial and final empty-channel powers. The duration of steady flow appears shorter for transmittance measurements (~5 s) than for load cell measurements (~10 s). This disparity is because of hysteresis induced by the relatively long time constant (~1.8 s) of the thermopile. Tests at various heights, z, show that transmittance increases significantly along the flow direction. This stems from a decrease in solid volume fraction with increasing z values. At equivalent heights, the transmittance is larger for the 2 mm particles than for 1 mm particles, consistent with the smaller mass flow rates measured for the former. Further tests (not shown) at various initial light source powers, P_0, were conducted to verify that the transmittance was independent of the light source intensity.

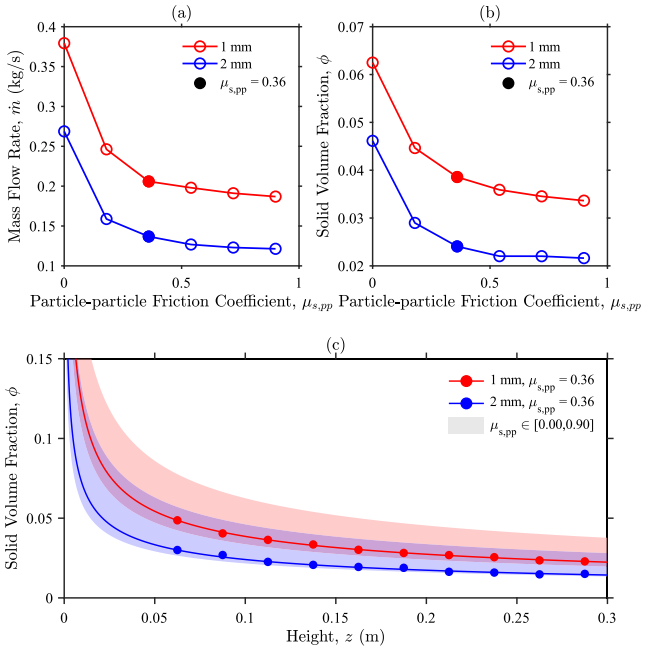

Fig. 8. Sensitivity test of (a) mass flow rate and (b) solid volume fraction to particle–particle coefficient of static friction at $z = 0.1$ m; (c) solid volume fraction range for 1 mm and 2 mm particles with particle–particle frictional coefficient $\mu_{s,pp}$ ranging from 0 to 0.9. All baseline parameters are listed in Table 3.

3.2. DEM simulations

Fig. 7 shows a qualitative comparison of DEM simulations with snapshots of particle positions captured by the high-speed camera at steady state. Apart from the slight non-uniformity in the experimental results due to a manufacturing defect, these images qualitatively match well with the predicted spatial distribution and the corresponding local solid volume fractions of particles. This lends further credibility to this approach and parameter selection for the DEM simulations. Models predict mass flow rates of 0.206 kg/s and 0.137 kg/s for 1 mm and 2 mm particles, respectively, which is within 10.43% and 14.37% of the measured values (Section 3.1), respectively. This deviation is attributed to the manufacturing irregularities in the width of the discharge slot, which cause the modeled overall slot area (which in turn governs the flow rate), to differ from the experimental overall slot area. This is because the modeled geometry uses the center slot width, W_s (Table 1). If instead the average slot width, $\overline{W}_s$, is used, a significantly improved prediction within 5% of measurements is observed. All DEM model results for solid volume fractions hereafter are however obtained considering the center slot width to better match the geometry where thermopile transmittance measurements are obtained.

A sensitivity analysis of the predicted mass flow rate and solid volume fraction to the particle–particle coefficient of static friction was performed to calibrate the DEM model to experiments. Fig. 8 shows the results of this analysis, where the solid volume fraction is measured at a representative location near the top of the channel ($z = 0.1$ m). The tested coefficients of static friction ranged from 0 to 0.9, and steady-state values are shown in Fig. 8. Both the mass flow rate and solid volume fraction decrease more steeply initially when $\mu_{s,pp}$ increases from 0 to 0.5. At $\mu_{s,pp} = 0.5$, the mass flow rate is ~50% lower than at $\mu_{s,pp} = 0$. For further increases in the friction coefficient, the mass flow rate and solid volume fraction converge asymptotically to a value.

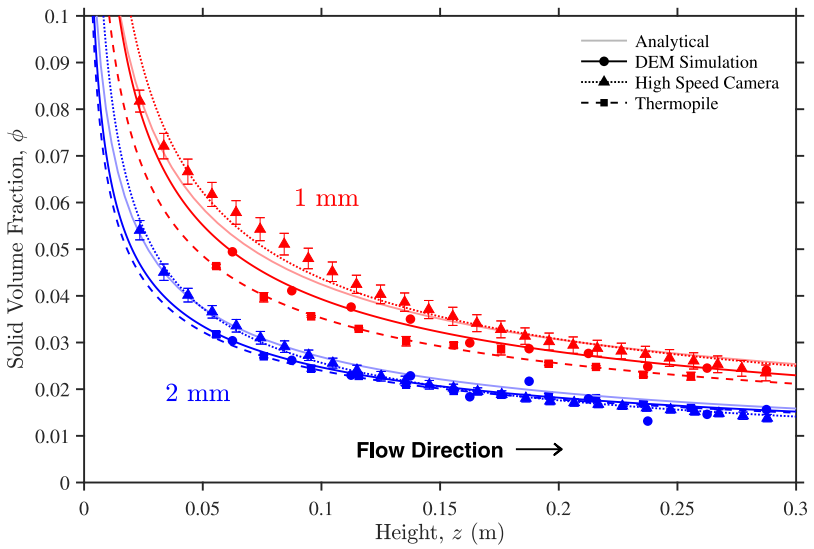

Fig. 9. Integrated comparison of experimental and modeling results for solid volume fraction as a function of height in a gravity-driven particle curtain for 1 and 2 mm particles. All plotted lines represent power law curve fits, intended to visually guide the connection between data. Thermopile and high-speed camera error bars are based on a 95% confidence interval in the transmittance measurements over four and six trials respectively at every z location.

With increasing friction coefficient, particles entering the channel lose more momentum through more intensive inter-particle interactions and thus decrease the mass flow rate. Particles spread out along the flow direction under gravity and then are less affected by friction. Friction, as a damping effect against gravity, indicates a lower acceleration rate for rough particles compared to smooth particles. Hence, the velocities for high-friction particles would increase slower and are prone to have lower solid volume fractions. However, the decreasing trend levels off after $\mu_{s,pp} = 0.5$. For particle curtain flows with relatively insignificant inter-particle contacts, most particles are already subject to small tangential forces compared to the normal forces. Therefore, increases in the static friction coefficient beyond a threshold value lead to fewer sliding events and have diminishing effects on the flow behavior. In summary, both the mass flow rate and solid volume fraction are most sensitive to the particle–particle frictional coefficient when it is lower than 0.5; beyond this value, they are less sensitive to this parameter.

From the sensitivity study, $\mu_{s,pp} = 0.36$ was selected as the best value to draw comparisons between model predictions and experimental evaluations. From the range of values examined, this friction coefficient minimized error for both mass flow rate and for the estimated range of solid volume fractions from the thermopile measurements. Additionally, the same value of $\mu_{s,pp} = 0.36$ led to a good match between predictions and measurements for both particle sizes tested. Even though this best-fit value is reasonably close to the reported data (0.5–0.72) for commercial proppants considered for CSP applications [48, 57], the porcelain particles investigated in this study are different from these in chemical composition and surface finish. Therefore, a direct comparison of this value against literature data is non-trivial.

3.3. Comparison of measurements and model predictions

Fig. 9 shows a comparison of the solid volume fractions obtained from the different measurement and modeling techniques. Note that for the experimental methods, solid volume fraction was calculated from raw transmittance by finding the roots of the nonlinear system described in Section 2.1.3. Raw transmittance data is given in Fig. 6 for the thermopile and Fig. B.1 for the high-speed camera. All methods predict similar trends of decreasing solid volume fraction along the flow direction and a reduction in the solid volume fraction with an increase in particle size. For all datasets, the solid volume fraction is lower for the larger particle size at all heights, z, which is consistent with the lower flow rates measured for the larger particles; from Eq. (7), it is expected that ϕ is proportional to $\dot{m}$. For any particle size, the solid volume fraction decreases following a power law relationship along the flow direction as particles spread out due to gravitational acceleration.

Measurements from the two experimental methods differed the most, with model predictions falling between them. Thermopile-derived solid volume fractions, computed here with Beer's law and a scaling function to account for dependent scattering effects (Section 2.1.3), are consistently the smallest for both particle sizes. Note that thermopile error bars are based on a 95% confidence interval over four trials at every z location. Conversely, front-lit high-speed camera-derived solid volume fractions are consistently the largest. This is because the image processing binarization scheme is equivalent to treating the particles as totally absorbing, which ignores scattering from particle surfaces and results in a lower transmittance than the thermopile. Of all datasets, the front-lit high-speed camera data has the greatest trial-to-trial variation. Moreover, the high-speed camera data display the greatest absolute deviation in solid volume fraction from the anticipated inverse square law—up to 0.27% (absolute) near $z = 0.07$ m. In that region, the fitted curve does not pass through the error bars, which are computed from a 95% confidence interval for the standard deviation of transmittance across six high-speed camera videos. This localized effect is attributed to a higher glare on the chamber window at this point, where the binarization scheme was qualitatively observed to perform worst.

Compared to the thermopile measurements and the DEM simulations, predictions from the single-particle model and the processed images from the high-speed camera overestimate ϕ, especially for the 1 mm particles. The R–T–B–N correlation using Eqs. (7) and (8) matches measured mass flow rates within 1.2% and 9.4%, respectively, for the 1 mm and 2 mm particles. The larger error for the 2 mm particles is attributed to the increase in the particle size relative to the hopper discharge slot width, which lowers the accuracy/effectiveness of the R–T–B–N correlation [51]. The overprediction of ϕ from this model is primarily because it precludes the effects of inter-particle interactions in the force calculations and does not account for manufacturing defects and tolerances. Finally, the DEM results match experimental measurements to within 12%. However, these results are specific to chosen model parameters, especially the coefficient of static friction (Table 3).

Overall, the comparisons in Fig. 9 reveal that there is reasonable convergence in the estimated solid volume fractions across different techniques.

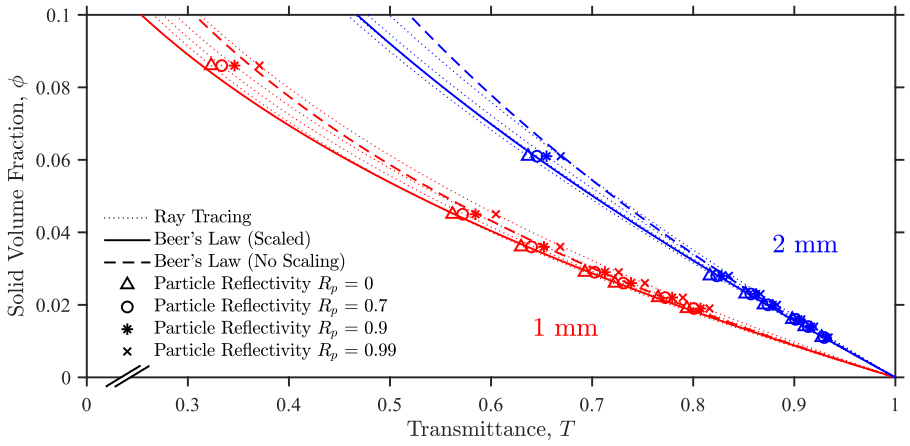

Fig. 10. Dependence of the relationship between transmittance and solid volume fraction on particle reflectivities based on ray tracing simulations (dotted lines, markers). For comparison, Beer's law (Eqs. (1)–(3)) with (solid) and without (dashed) scale factor S_ϕ, which respectively model dependent scattering and independent scattering effects, are included.

3.4. Ray tracing and optical property dependence

To probe the effects of particle reflectivity, R_p, on the relationship between transmittance and solid volume fraction, Monte Carlo ray tracing simulations were performed. These are direct simulations that track intersections of rays with particles present at locations obtained from snapshots in the DEM model and hence dependent scattering effects are intrinsically factored in these calculations. Results are presented in Fig. 10 and are compared with predictions obtained from Beer's law equations with and without dependent scattering effects (Eqs. (2) and (3), respectively). These results reveal that as the particle reflectivity increases, the solid volume fraction to yield a fixed transmittance also increases. Therefore, when the measured transmittance from the thermopile is used to obtain a solid volume fraction, particle reflectivity plays an important role, especially when the measured transmittance is small.

The difference between independent and dependent scattering is more pronounced when transmittance decreases and the corresponding solid volume fraction increases. The comparison between the unscaled Beer's law (dashed line) and the ray tracing results (dotted line) reveals a larger difference for the 2 mm particles than the 1 mm ones. This dependence may arise as a consequence of the small ratio between the channel width and the particle diameter, which can cause further deviations from the random or Poissonian spatial distribution of particles assumed by Beer's law. Furthermore, the solid volume fraction at a given transmittance changes with R_p because of scattering due to reflections in the particle curtain; Beer's law does not account for this effect. Indeed, for highly reflective particles, Beer's law with dependent scattering effects, Eq. (3), underestimates the solid volume fraction at a given transmittance.

The results generated from Monte Carlo ray tracing simulations (Fig. 10) are applied to obtain a new, reflectivity-dependent scale factor, S_R in Eq. (11), applied alongside S_ϕ in Eq. (3), to relate transmittance and solid volume fraction:

$$S_R = 0.13\sqrt{1 - R_p} + 0.87 \tag{11}$$

The dependence of the reflectivity scale factor on the particle reflectivity (Eq. (11)) is obtained by using the ray tracing datasets with the MATLAB curve fitting toolbox, yielding good quality fits ($R^2 = 0.99$). The square root dependence of transmittance with $1 - R_p$ is consistent with closed-form solutions obtained for transmittance in one-dimensional participating media [58]. For perfectly absorbing particles, S_R has a limiting value of 1 which leads to the traditional Beer's law expression in Eq. (1).

Combined, a modified, closed-form expression (Eq. (12)) is proposed to relate transmittance and solid volume fraction in particle-flow measurements that accounts for dependent scattering effects as well as particle reflectivities with a collimated incident light source:

$$T = \exp(-S_\phi S_R \tau_W) \quad \text{where} \quad \tau_W = \beta_{\text{ind}} W \tag{12}$$

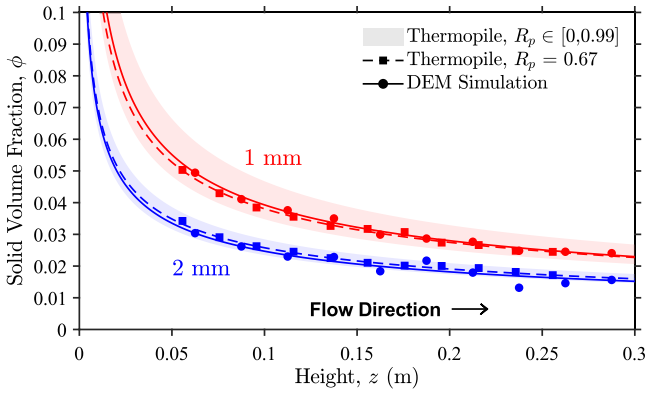

Fig. 11. DEM results from Fig. 9 and experimental results rectified with a reflectivity-dependent scale factor, with the possible range of thermopile results given for particle reflectivities in the range $R_p \in [0, 0.99]$ indicated by the shaded regions.

Solid volume fractions derived from the thermopile measurements by applying the modified Beer's law expression (Eq. (12)) are presented in Fig. 11. The shaded region represents the variation in the estimated solid volume fraction for a range of particle reflectivities, $R_p \in [0, 0.99]$. The area of this region is larger for the smaller particle size due to the increased likelihood of light scattering/reflections with a larger ratio of the channel width to particle size. The relationship in Eq. (12) between transmittance and solid volume fraction is equally applicable for any particle size, curtain thickness, or optical properties.

The solid volume fractions calculated from the thermopile measurements using the new scale factor give exceptional agreement with the DEM results (within 5%) when assuming $R_p = 0.67$, based on the measured reflectance of a bed of porcelain particles. The best-fit values for R_p will change based on the assumption of diffuse/specular reflections on the particle surface; this study assumed diffuse reflections. This underscores the benefits of applying an improved radiative transport expression with the knowledge of particle optical properties to convert measured transmittance to a solid volume fraction.

3.5. Thermopile technique: merits and limitations

The proposed light source and thermopile detector technique marries dual advantages of low cost and ease of setup compared to other advanced transmittance-based techniques (e.g., X-ray, MRI, etc.). Moreover, the light source and detector assembly are much more compact than a camera setup and comparable to a capacitance-based measurement setup. This method also has a reasonably good spatial resolution ~1 cm. In contrast to capacitance and other optical techniques, no additional calibration is required when transforming the thermopile-measured transmittance to a solid volume fraction.

On the other hand, a limitation of this technique is its low time resolution (~1 s), which makes it challenging to apply for high-speed or unsteady particle flows. Another minor consideration is that if the particles are not strongly absorbing in the spectrum of the light source, the conversion of transmittance to solid volume fraction requires knowledge of the optical properties. This becomes an additional input parameter to characterize solid volume fractions and should inform the spectrum of the light source selected for a particular granular medium. This technique cannot be directly used for hot particle flows without separating the thermal emission of the walls and particles from the light source that is used. This could in theory be achieved with an appropriate filter in front of the thermopile that blocks thermal emission while allowing light from the source to pass. However, cold flow tests are expected to be sufficient as solid volume fractions are not expected to be a strong function of particle temperature for the curtain flow regime.

Even though this study has applied the thermopile technique to measure solid volume fractions less than 0.1, it can theoretically be applied for larger ϕ values. The standard deviation in the measured transmittance was averaged over data points obtained at various locations along the flow channel and for both particle sizes; this average deviation was $\Delta T = 0.32\%$. This trial-to-trial deviation is much larger than the systematic error specified for the detector and hence is assumed to be the minimum significant transmittance that can be measured with the thermopile. This corresponds to a maximum measurable solid volume fraction of ~0.45 with perfectly absorbing particles (Eq. (12)). However, the absolute error in the solid volume fraction is dependent on parameters other than the transmittance measurement error. In particular, it increases exponentially with the solid volume fraction, ϕ, and with the ratio of the width of the channel to the particle size, W/d_p, and proportionally to the measured error in the transmittance. Moreover, if the particles are more reflective, even larger solid volume fractions can be measured for the same minimum transmittance. A quantitative supporting discussion relating these error calculations is provided in Appendix E. By assuming the trial-to-trial transmittance error to be agnostic to the flow regime (equivalently, the solid volume fraction), Fig. E.1 shows that for a nominal channel width that is 5 times the particle diameter, $W/d_p = 5$, the absolute error is less than 2% even for dense flows with solid volume fraction of $\phi = 0.5$. However, when the relative curtain width $W/d_p = 10$, the maximum solid volume fraction that can be measured within the same 2% absolute error is 0.3.

Moreover, the maximum solid volume fraction measured in these experiments are limited by other factors including the thermopile detector housing size and the nature of the curtain flow regime. The thermopile detector with its housing is 0.07 m in diameter, so it was not practical to place the thermopile at the very top of the channel near the slide gate. In the curtain flow investigated, the largest drop in the solid volume fractions is expected in the first 15 cm from the top slide gate for the millimeter-sized particles, and this drop occurs even more rapidly for smaller particles. Therefore, even if 100 μm sized particles were measured in the flow channel, it is expected from analytical model predictions that the first location of measurement with the thermopile will still yield solid volume fractions less than 0.15.

Overall, the thermopile-based transmittance approach to estimate solid volume fraction shows promise to be applicable even for denser flows of particles, especially with the use of more reflective than absorptive particles in the spectrum of the light source.

4. Summary and conclusions

This study successfully demonstrates the use of a thermopile detector paired with a visible light source to determine solid volume fractions along the flow direction for gravity-driven particle flows. A hopper-channel test stand, with chamber dimensions of 9.58 mm × 150 mm × 500 mm (L × W × H), was designed and fabricated to characterize the flow of porcelain particles (1 and 2 mm diameter). Light transmitted was measured at eleven positions along the flow direction. Front-lit high-speed images of the same setup were also obtained to compare results across different measurement techniques. To support and interpret experimental data, an analytical model and a discrete element model for Lagrangian particle tracking were implemented. Additionally, Monte Carlo ray tracing simulations were performed together with particle flow simulations to inform the governing relationship between transmittance, solid volume fraction, and particle optical properties.

All experimental data show very good agreement with the models. All methods show that the solid volume fraction decreases along the flow direction following a power law relationship and that the dip is larger for the 1 mm particles than the 2 mm ones. Qualitatively, snapshots of the flow captured in DEM simulations and by the high-speed camera show very similar flow profiles. Sensitivity analyses performed on the DEM model show a significant influence of the particle–particle static friction coefficient on both the mass flow rate and the predicted solid volume fraction distributions. The measured steady flow rates of 0.230 and 0.160 kg/s for the 1 and 2 mm particles, respectively, match those found with empirical correlations and DEM simulations within 10%.

Distinct from the DEM simulations that directly calculate solid volume fractions, the thermopile and high-speed imaging techniques rely on transforming the measured transmittance to a solid volume fraction. Ray tracing simulations inform the development of a new, effective, and simple closed-form expression to relate transmittance, solid volume fraction, and additionally, particle reflectivity. This leads to a much closer match of within 5% between the thermopile estimations and DEM simulations for solid volume fractions for both particle sizes tested.

On the whole, thermopile-based transmittance measurements are a promising approach to optically characterize particle flows. The technique is reliable, low-cost, and accessible with good spatial resolution. It is also compatible with different test setups and materials, including alternative photodetectors that could further improve the cost and time resolution of the measurements.

Through systematic analyses, less than 2% absolute error is projected in solid volume fractions even up to 0.45 for a channel width to particle diameter ratio of 5. The use of more reflective particles with the same flow chamber design can further increase the range of accessible solid volume fractions through transmittance measurements.

CRediT authorship contribution statement

Theo A. Rulko: Conceived this study, Designed and built the experimental test stand, Performed the majority of the experiments in the study and related data analyses, Writing, Data interpretation and revisions. **Bingjia Li:** Developed DEM models and performed related data analyses, Writing, Data interpretation and revisions. **Brandon Surhigh:** Performed the majority of the experiments in the study and related data analyses, Writing, Data interpretation and revisions. **J. Michael Mayer:** Conceived this study, Designed and built the experimental test stand, Performed reflectance measurements for particles, Overall project management, Writing, Data interpretation and revisions. **Rohini Bala Chandran:** Conceived this study, Overall project management, Secured funding for the project, Writing, Data interpretation and revisions.

Declaration of competing interest

The authors declare that they have no known competing financial interests or personal relationships that could have appeared to influence the work reported in this paper.

Data availability

The data for results presented in Figs. 8–11 and Appendices B–E are reported here: https://doi.org/10.17632/n69bss6bfg. Additionally, videos of flowing particles from experiments and simulations are included in the same repository.

Acknowledgments

Rulko, Li, and Bala Chandran acknowledge funding from the National Science Foundation under Grant No. 2144184. Li was also supported by the Donors of the American Chemical Society Petroleum Research Fund (ACS-PRF, 62639-DNI9). Surhigh and Mayer were partially funded by the U.S. Department of Energy's Office of Energy Efficiency and Renewable Energy (EERE) under the Solar Energy Technologies Office (SETO) award number DE-EE0009819. The authors are grateful for the support of Prof. Margret Wooldridge at the University of Michigan, who loaned the Vision Research Phantom v711 camera used in this work, and to her doctoral student, Varun Chakrapani, for assistance with operating the camera. The authors would also like to acknowledge Loadstar Sensors for providing an educational discount on the load cell used in this work.

Appendix A. Measurement of particle density and size distributions

Particle density was found by measuring the mass and volume of roughly 10,000 particles and taking the ratio. Mass was found with a laboratory centigram balance, while volume was found using the water displacement method. Particle density, ρ_p, was found to be 2650 kg/m^3 for both 1 and 2 mm particles.

Analysis of the size distribution of the roughly 1 mm and 2 mm particles was conducted using image processing techniques in MATLAB. For each particle size, several photos of the particles spread out on a black surface were taken, with a ruler visible in the frame to set a length scale, as shown in Fig. A.1a. Together, roughly 12,000 particles of each size were imaged. In MATLAB, a scale factor was computed for each image based on the length of the ruler. Individual particles were identified via a circular Hough Transform-based algorithm [59], and this algorithm was implemented using MATLAB's `imfindcircles`, a function provided by the Image Processing Toolkit. This is shown in Fig. A.1b. The diameter of each particle identified was tabulated and used to generate the histograms shown in Fig. A.1c. Normal distributions were fit to the histograms, and the mean and standard deviation of each particle size distribution were found. Mean values from these size distributions of 1.21 mm and 2.18 mm were obtained for particles with nominal diameters of 1 mm and 2 mm, respectively. The accuracy of this method was verified by photographing a representative sample of particles, directly measuring their diameter with a micrometer, and verifying that the diameter reported in MATLAB matched to within the measurement error of the micrometer.

Appendix B. Transmittance data captured using the high-speed camera

Opacity data is obtained from each frame of the high-speed camera. These data are time-averaged to obtain a single, quasi-steady measurement. The shaded region in Fig. B.1 represents the spread of data obtained over all frames, which is considered to be statistical noise. The red dots represent the average measurement in each bin, the quantity used in solid volume fraction calculations.

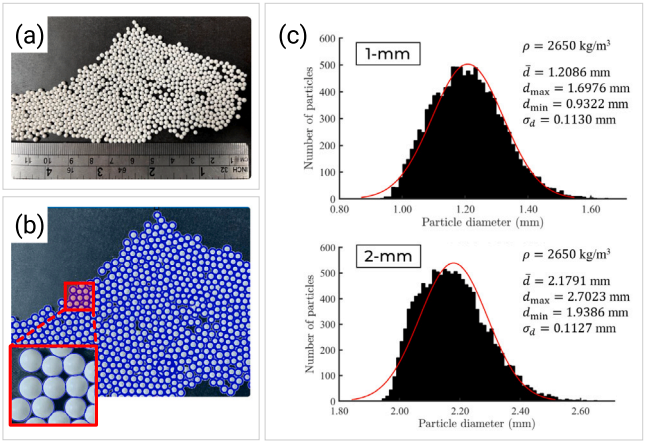

Fig. A.1. Overview of the methods and results for the particle size distribution analysis. (a) Sample photograph of 2 mm particles; (b) particles in the image identified in MATLAB and indicated with blue circles; (c) particle size distributions and statistics for 1 mm and 2 mm particles.

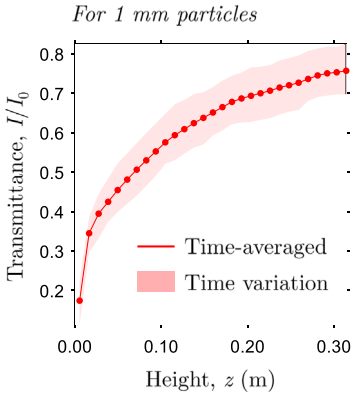

Fig. B.1. Transmittance plot from processed high-speed camera data for 1 mm particles. Frame-to-frame variance is shown by shading.

Appendix C. Sensitivity of DEM results to particle size distributions

Fig. C.1 shows the predicted solid volume fraction as a function of height for a monodisperse particle size distribution compared against the normal size distribution measured in Appendix A. Note that the critical timestep of the DEM simulation is directly proportional to the minimum particle diameter. Therefore, this critical time step is reduced by 23% for the monodisperse simulations. The results show that, for both sizes of particles, the difference between predictions computed using the monodisperse and normal distributions at each height is within 5%. This validates the choice of using a uniform particle size obtained from the mean value of the measured size distributions for all subsequent DEM simulations in this study.

Appendix D. Reflectivity measurements of particle beds

The reflectivity of the particles was quantified by performing measurements in a UV–Vis spectrophotometer. Packed beds of the particles were loaded into a sample holder and placed into a diffuse reflectance accessory for measurement (Fig. D.1). Reflectivity was calculated by referencing the reflected signal of the particles to a background of barium sulfate ($BaSO_4$) powder and shows no dependence on particle size. The reflectivity is low in the ultraviolet (UV), but increases from ~10% to ~50% as the wavelength goes from 300 nm to 400 nm. Across

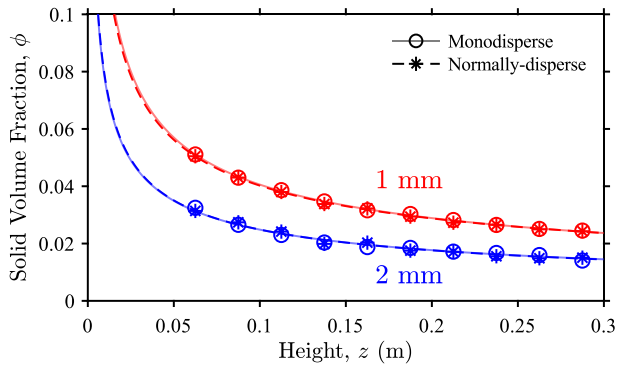

Fig. C.1. DEM modeling results for solid volume fraction as a function of height for 1 mm and 2 mm particles with mono- and normally-dispersed size distributions. Plotted lines represent the power law curve fits to data points. In all cases, the monodisperse results show good agreement with the normally-dispersed results.

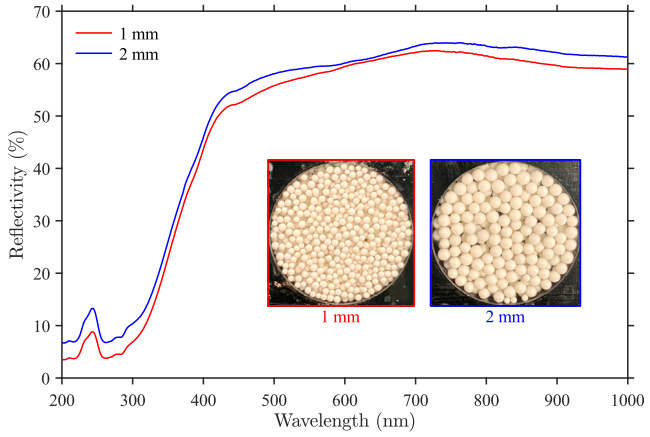

Fig. D.1. Reflectivity of particle beds composed of 1 mm and 2 mm particles for a wavelength range of 200–1000 nm.

the visible spectrum (400–700 nm), which contains the majority of the energy emitted by the light source used in this study, the reflectivity mostly lies between 50% and 60%. In the near-IR (> 700 nm), the reflectivity is consistently around 60%. The measured reflectivity for the particle beds is expected to underestimate the reflectivity of the particle surfaces due to multiple scattering events by the packed bed. Thus, 60% is considered to be a lower bound for a particle surface reflectivity. This is consistent with the 67% reflectivity value that most closely matches the thermopile data to the DEM modeling data (Fig. 11).

Appendix E. Error analysis for solid volume fractions obtained from transmittance measurements

Measurement error in the transmittance obtained from the thermopile detector is propagated to obtain the error in the derived solid volume fraction based on the Beer's law relationship, Eq. (1). Therefore, the error in ϕ varies with particle size, d_p, curtain width, W, and the mean transmittance measured, T_m and its corresponding solid volume fraction, ϕ. For the sake of simplicity, error propagation is applied by assuming the scale factors due to dependent scattering and particle reflectivity, S_ϕ and S_R, to be 1. This is expected to lead to conservatively large uncertainty values in ϕ, $\Delta\phi$:

$$T_m = \exp\left(-\frac{3\phi}{2d_p}\cdot W\right) \Longrightarrow \phi = \frac{-2d_p}{3W}\ln(T_m) \tag{E.1}$$

$$\Delta\phi = \frac{-2d_p}{3T_m W}\Delta T \tag{E.2}$$

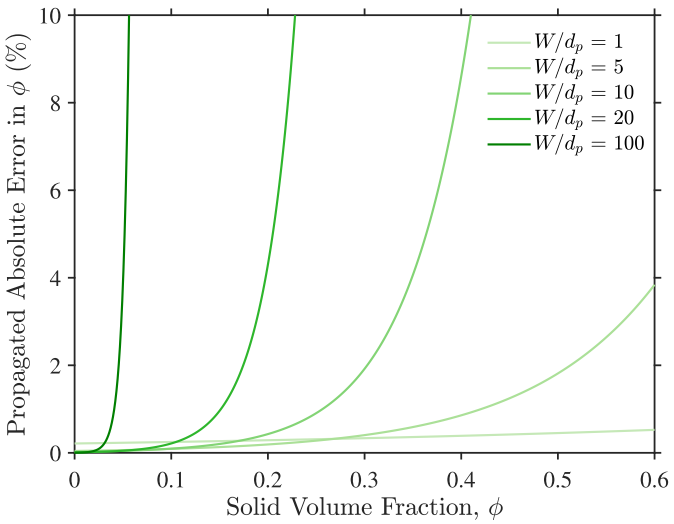

Fig. E.1. Propagated absolute error as a percentage in solid volume fraction for various solid volume fractions, ϕ, as a function of the ratio of channel width to the particle diameter, W/d_p. $|\Delta\phi|$ values are obtained based on the transmittance measurement trial-to-trial error of $|\Delta T| = 0.32\%$ and using Eq. (E.3).

Substituting Eq. (E.1) into (E.2) and simplifying:

$$|\Delta\phi| = \frac{2d_p}{3W}\exp\left(\frac{3\phi W}{2d_p}\right)|\Delta T| \tag{E.3}$$

Therefore, Eq. (E.2) relates trial-to-trial measurement error in transmittance in the thermopile, ΔT, with an error in the solid volume fraction, $\Delta\phi$. Fig. E.1 illustrates the dependence of this error on the geometric parameters, W and d_p, and as a function of the solid volume fraction deduced from the measured transmittance. In this plot, ΔT is the standard deviation in the measured transmittance over many experimental trials, and is 0.32%. Therefore, the resulting error, $\Delta\phi$, for the solid volume fraction is also an absolute and a percentage quantity.

References

[1] K.J. Albrecht, C.K. Ho, Design and operating considerations for a shell-and-plate, moving packed-bed, particle-to-sCO2 heat exchanger, Sol. Energy 178 (2019) 331–340, http://dx.doi.org/10.1016/j.solener.2018.11.065.

[2] C.K. Ho, K.J. Albrecht, L. Yue, B. Mills, J. Sment, J. Christian, M. Carlson, Overview and design basis for the Gen 3 particle Pilot Plant (G3P3), in: AIP Conference Proceedings, vol. 2303, 2020, 030020, http://dx.doi.org/10.1063/5.0029216.

[3] H. Zhang, H. Benoit, D. Gauthier, J. Degrève, J. Baeyens, I.P. López, M. Hemati, G. Flamant, Particle circulation loops in solar energy capture and storage: Gas–solid flow and heat transfer considerations, Appl. Energy 161 (2016) 206–224, http://dx.doi.org/10.1016/j.apenergy.2015.10.005.

[4] J.J. Nieuwland, R. Meijer, J.A.M. Kuipers, W.P.M. van Swaaij, Measurements of solids concentration and axial solids velocity in gas-solid two-phase flows, Powder Technol. 87 (2) (1996) 127–139, http://dx.doi.org/10.1016/0032-5910(95)03081-6.

[5] U. Arena, A. Cammarota, L. Massimilla, D. Pirozzi, The hydrodynamic behavior of two circulating fluidized bed units of different sizes, in: Proceedings of the Second International Conference on Circulating Fluidized Beds, Elsevier, 1988, pp. 223–230, http://dx.doi.org/10.1016/b978-0-08-036225-0.50025-3.

[6] H. Benoit, I.P. López, D. Gauthier, G. Flamant, Temperature influence on wall-to-particle suspension heat transfer in a solar tubular receiver, in: AIP Conference Proceedings, vol. 1734, 2016, 040002, http://dx.doi.org/10.1063/1.4949093.

[7] G. Flamant, D. Gauthier, H. Benoit, J.-L. Sans, R. Garcia, B. Boissière, R. Ansart, M. Hemati, Dense suspension of solid particles as a new heat transfer fluid for concentrated solar thermal plants: On-sun proof of concept, Chem. Eng. Sci. 102 (2013) 567–576, http://dx.doi.org/10.1016/j.ces.2013.08.051.

[8] R.A. Cocco, S.B.R. Karri, T.M. Knowlton, J. Findlay, T. Gauthier, J.W. Chew, C.M. Hrenya, Intrusive probes in riser applications, AIChE J. 63 (12) (2017) 5361–5374, http://dx.doi.org/10.1002/aic.15892.

[9] E.-U. Hartge, Y. Li, J. Werther, Analysis of the local structure of the two phase flow in a fast fluidized bed, in: Proceedings of the First International Conference on Circulating Fluidized Beds, Elsevier, 1986, pp. 153–160, http://dx.doi.org/10.1016/b978-0-08-031869-1.50018-1.

[10] E.-U. Hartge, D. Rensner, J. Werther, Solids concentration and velocity patterns in circulating fluidized beds, in: Proceedings of the Second International Conference on Circulating Fluidized Beds, Elsevier, 1988, pp. 165–180, http://dx.doi.org/10.1016/b978-0-08-036225-0.50020-4.

[11] H. Johnsson, F. Johnsson, Measurements of local solids volume-fraction in fluidized bed boilers, Powder Technol. 115 (1) (2001) 13–26, http://dx.doi.org/10.1016/s0032-5910(00)00270-9.

[12] F. Taghipour, N. Ellis, C. Wong, Experimental and computational study of gas–solid fluidized bed hydrodynamics, Chem. Eng. Sci. 60 (24) (2005) 6857–6867, http://dx.doi.org/10.1016/j.ces.2005.05.044.

[13] A. Frankel, G. Iaccarino, A. Mani, Convergence of the Bouguer–Beer law for radiation extinction in particulate media, J. Quant. Spectrosc. Radiat. Transfer 182 (2016) 45–54, http://dx.doi.org/10.1016/j.jqsrt.2016.05.009.

[14] R.J. Braham, A.T. Harris, A complete multi-scale simulation of light absorption within a fluidized bed photoreactor using integrated particle, fluid and photon behaviour models, Phys. Chem. Chem. Phys. 15 (29) (2013) 12373–12385, http://dx.doi.org/10.1039/c3cp50328c.

[15] K.O. Fong, F. Coletti, Experimental analysis of particle clustering in moderately dense gas–solid flow, J. Fluid Mech. 933 (2022) A6, http://dx.doi.org/10.1017/jfm.2021.1024.

[16] P. Gougeon, J.N.L. Toulouzan, G. Gouesbet, C. Thenard, Optical measurements of particle size and concentration in densely laden media using a visible/infrared double extinction technique, J. Phys. E: Sci. Instrum. 20 (10) (1987) 1235–1242, http://dx.doi.org/10.1088/0022-3735/20/10/018.

[17] J. Link, C. Zeilstra, N. Deen, H. Kuipers, Validation of a discrete particle model in a 2D spout-fluid bed using non-intrusive optical measuring techniques, Can. J. Chem. Eng. 82 (1) (2008) 30–36, http://dx.doi.org/10.1002/cjce.5450820105.

[18] J.D. Ortega, G. Anaya, P. Vorobieff, G. Mohan, C.K. Ho, Imaging particle temperatures and curtain opacities using an IR camera, in: ASME 2020 14th International Conference on Energy Sustainability, American Society of Mechanical Engineers, 2020, V001t02a018, http://dx.doi.org/10.1115/es2020-1688.

[19] L. Qian, Y. Lu, W. Zhong, X. Chen, B. Ren, B. Jin, Developing a novel fibre high speed photography method for investigating solid volume fraction in a 3D spouted bed, Can. J. Chem. Eng. 91 (11) (2013) 1793–1799, http://dx.doi.org/10.1002/cjce.21915.

[20] B. Spinewine, H. Capart, M. Larcher, Y. Zech, Three-dimensional voronoï imaging methods for the measurement of near-wall particulate flows, Exp. Fluids 34 (2) (2003) 227–241, http://dx.doi.org/10.1007/s00348-002-0550-4.

[21] L. Babout, K. Grudzien, E. Maire, P.J. Withers, Influence of wall roughness and packing density on stagnant zone formation during funnel flow discharge from a silo: An X-ray imaging study, Chem. Eng. Sci. 97 (2013) 210–224, http://dx.doi.org/10.1016/j.ces.2013.04.026.

[22] M. Bieberle, F. Barthel, Combined phase distribution and particle velocity measurement in spout fluidized beds by ultrafast X-ray computed tomography, Chem. Eng. J. 285 (2016) 218–227, http://dx.doi.org/10.1016/j.cej.2015.10.003.

[23] M. Mehdizad, L. Fullard, P. Galvosas, D. Holland, Quantitative measurements of flow dynamics in 3D hoppers using MRI, Powder Technol. 392 (2021) 69–80, http://dx.doi.org/10.1016/j.powtec.2021.06.048.

[24] R. Stannarius, D.S. Martinez, T. Börzsönyi, M. Bieberle, F. Barthel, U. Hampel, High-speed x-ray tomography of silo discharge, New J. Phys. 21 (11) (2019) 113054, http://dx.doi.org/10.1088/1367-2630/ab5893.

[25] S. Waktola, A. Bieberle, F. Barthel, M. Bieberle, U. Hampel, K. Grudzień, L. Babout, A new data-processing approach to study particle motion using ultrafast X-ray tomography scanner: Case study of gravitational mass flow, Exp. Fluids 59 (4) (2018) 69, http://dx.doi.org/10.1007/s00348-018-2523-2.

[26] C.R.K. Windows-Yule, J.P.K. Seville, A. Ingram, D.J. Parker, Positron emission particle tracking of granular flows, Annu. Rev. Chem. Biomol. Eng. 11 (2020) 367–396, http://dx.doi.org/10.1146/annurev-chembioeng-011620-120633.

[27] P. Tortora, J. Torczynski, S. Ceccio, The Equivalent Electrical Permittivity of Gas-Solid Mixtures At Intermediate Solid Volume Fractions, Tech. Rep., Sandia National Laboratories (SNL), Albuquerque, NM, and Livermore, CA (United States), 2005, http://dx.doi.org/10.2172/876324.

[28] D.L. George, J.R. Torczynski, K.A. Shollenberger, T.J. O'Hern, S.L. Ceccio, Validation of electrical-impedance tomography for measurements of material distribution in two-phase flows, Int. J. Multiph. Flow. 26 (4) (2000) 549–581, http://dx.doi.org/10.1016/s0301-9322(99)00029-4.

[29] B. Hage, J. Werther, K. Narukawa, S. Mori, Capacitance probe measurement technique for local particle volume concentration in circulating fluidized bed combustors, J. Chem. Eng. Jpn. 29 (4) (1996) 594–602, http://dx.doi.org/10.1252/jcej.29.594.

[30] K. Kim, N. Siegel, G. Kolb, V. Rangaswamy, S.F. Moujaes, A study of solid particle flow characterization in solar particle receiver, Sol. Energy 83 (10) (2009) 1784–1793, http://dx.doi.org/10.1016/j.solener.2009.06.011.

[31] C. Rautenbach, R.F. Mudde, X. Yang, M.C. Melaaen, B.M. Halvorsen, A comparative study between electrical capacitance tomography and time-resolved X-ray tomography, Flow Meas. Instrum. 30 (2013) 34–44, http://dx.doi.org/10.1016/j.flowmeasinst.2012.11.005.

[32] N. Siegel, G. Kolb, K. Kim, V. Rangaswamy, S. Moujaes, Solid particle receiver flow characerization studies, in: Proceedings of ES2007, ASME 2007 Energy Sustainability Conference, 2007, pp. 877–883, http://dx.doi.org/10.1115/es2007-36118.

[33] P.R. Tortora, S.L. Ceccio, A.G. Mychkovsky, T.J. O'Hern, J.R. Torczynski, Radial profiles of solids loading and flux in a gas–solid circulating fluidized bed, Powder Technol. 180 (3) (2008) 312–320, http://dx.doi.org/10.1016/j.powtec.2007.09.007.

[34] D. Wang, M. Xu, Q. Marashdeh, B. Straiton, A. Tong, L.-S. Fan, Electrical capacitance volume tomography for characterization of gas–solid slugging fluidization with geldart group D particles under high temperatures, Ind. Eng. Chem. Res. 57 (7) (2018) 2687–2697, http://dx.doi.org/10.1021/acs.iecr.7b04733.

[35] J.N. Sines, S. Hwang, Q.M. Marashdeh, A. Tong, D. Wang, P. He, B.J. Straiton, C.E. Zuccarelli, L.-S. Fan, Slurry bubble column measurements using advanced electrical capacitance volume tomography sensors, Powder Technol. 355 (2019) 474–480, http://dx.doi.org/10.1016/j.powtec.2019.07.077.

[36] A.K.R. Choudhury, Principles of colour and appearance measurement: Object appearance, colour perception and instrumental measurement, in: Woodhead Publishing Series in Textiles, Elsevier Science, 2014, pp. 65–69, http://dx.doi.org/10.1533/9780857099242.53, (Chapter 2.6 - Laws of absorption).

[37] Lyman Products: Raytech Division, Safety data sheet: Porcelain balls finishing media, (5) 2019, Rev. 1.

[38] LoadStar Sensors, Iweigh USB scale, 2014.

[39] Neewer, NL480 bi-color LED panel light, (Nl480) 2021.

[40] Newport Corporation, 919P series thermopile sensors, (Ds-051303) 2018.

[41] D.D. Pollock, Thermoelectricity - Theory, Thermometry, Tool, American Society for Testing and Materials, 1985.

[42] C.K. Ho, S. Kinahan, J.D. Ortega, P. Vorobieff, A. Mammoli, V. Martins, Characterization of particle and heat losses from falling particle receivers, in: ASME 2019 13th International Conference on Energy Sustainability, American Society of Mechanical Engineers, 2019, V001t03a001, http://dx.doi.org/10.1115/es2019-3826.

[43] Otsu, A threshold selection method from Gray-level histograms, IEEE Trans. Syst. Man Cybern. 9 (1) (1979) 62–66.

[44] K. Kamiuto, S. San Yee, Correlated radiative transfer through a packed bed of opaque spheres, Int. Commun. Heat Mass Transfer 32 (1–2) (2005) 133–139, http://dx.doi.org/10.1016/j.icheatmasstransfer.2004.03.021.

[45] B.P. Singh, M. Kaviany, Independent theory versus direct simulation of radiation heat transfer in packed beds, Int. J. Heat Mass Transfer 34 (11) (1991) 2869–2882, http://dx.doi.org/10.1016/0017-9310(91)90247-c.

[46] B.P. Singh, M. Kaviany, Modelling radiative heat transfer in packed beds, Int. J. Heat Mass Transfer 35 (6) (1992) 1397–1405, http://dx.doi.org/10.1016/0017-9310(92)90031-m.

[47] B. Li, R. Bala Chandran, Effects of spatial correlations in particulate media on dependent scattering and radiative transport, Int. J. Heat Mass Transfer 182 (2022) 121951, http://dx.doi.org/10.1016/j.ijheatmasstransfer.2021.121951.

[48] C. Chen, D. Ranjan, P.G. Loutzenhiser, Z.M. Zhang, A numerical study of the spectral radiative properties of packed bed with mixed bauxite and silica spheres, Int. J. Heat Mass Transfer 207 (2023) 124025, http://dx.doi.org/10.1016/j.ijheatmasstransfer.2023.124025.

[49] F.A. Morrison, An introduction to fluid mechanics, in: External flows, Cambridge University Press, 2013, pp. 600–738, (Chapter 8).

[50] K.K. Rao, P.R. Nott, An introduction to granular flow, in: Cambridge Series in Chemical Engineering, Cambridge University Press, 2008, http://dx.doi.org/10.1017/cbo9780511611513.

[51] R.M. Nedderman, Statics and Kinematics of Granular Materials, Cambridge University Press, 1992, http://dx.doi.org/10.1017/cbo9780511600043.

[52] F.A.L. Dullien, 3 - pore structure, in: Porous Media: Fluid Transport and Pore Structure, Academic Press, 1979, p. 132, http://dx.doi.org/10.1016/b978-0-12-223650-1.50008-5.

[53] C. Kloss, C. Goniva, A. König, S. Amberger, S. Pirker, Models, algorithms and validation for opensource DEM and CFD-DEM, Prog. Comput. Fluid Dyn. 12 (2012) 140–152, http://dx.doi.org/10.1504/pcfd.2012.047457.

[54] Z. Yan, S.K. Wilkinson, E.H. Stitt, M. Marigo, Discrete element modelling (DEM) input parameters: Understanding their impact on model predictions using statistical analysis, Comput. Part. Mech. 2 (3) (2015) 283–299, http://dx.doi.org/10.1007/s40571-015-0056-5.

[55] J. Hao, Y. Li, Y. Guo, H. Jin, J.S. Curtis, The effect of polydispersity on the stresses of cylindrical particle flows, Powder Technol. 361 (2020) 943–956, http://dx.doi.org/10.1016/j.powtec.2019.10.109.

[56] C.J. Coetzee, Review: Calibration of the discrete element method, Powder Technol. 310 (2017) 104–142, http://dx.doi.org/10.1016/j.powtec.2017.01.015.

[57] J. Grobbel, H. Kruggel-Emden, R. Pitz-Paal, Modeling Solar Particle Receivers with the Discrete Element Method (Ph.D. thesis), Rheinisch-Westfälische Technische Hochschule Aachen, Aachen, 2020, http://dx.doi.org/10.18154/rwth-2020-01764.

[58] K.C. Weston, J. Reynolds, A. Alikhan, D.W. Drago, Radiative Transfer in Highly Scattering Materials - Numerical Solution and Evaluation of Approximate Analytic Solutions, Tech. Rep., (19740021895) The University of Tulsa, Tulsa, OK, 1974, URL https://ntrs.nasa.gov/citations/19740021895.

[59] T. Atherton, D.J. Kerbyson, Size invariant circle detection, Image Vis. Comput. 17 (2001) 795–803, http://dx.doi.org/10.1016/s0262-8856(98)00160-7.